# Parallel Active Link Suspension: Full Car Application with Frequency-Dependent Multi-Objective Control Strategies

Min Yu, *Member, IEEE,* Simos A. Evangelou, *Senior Member, IEEE,* and Daniele Dini

***Abstract*—In this paper, a recently proposed at basic level novel suspension for road vehicles, the Parallel Active Link Suspension (PALS), is investigated in the realistic scenario of a SUV full car. The involved rocker-pushrod assembly is generally optimized to maximize the PALS capability in improving the suspension performance. To fully release the PALS functions of dealing with both low- and high-frequency road cases, a PID control scheme is firstly employed for the chassis attitude stabilization, focusing on the minimization of both the roll and pitch angles; based on a derived linear equivalent model of the PALS-retrofitted full car, an $H_\infty$ control scheme is designed to enhance the ride comfort and road holding; moreover, a frequency-dependent multi-objective control strategy, that combines the developed PID and $H_\infty$ control, is proposed to enable: i) chassis attitude stabilization at 0-1 Hz, ii) vehicle vibration attenuation at 1-8 Hz, and iii) control effort penalization (for energy saving) above 10 Hz. With a group of ISO-defined road events tested, numerical simulation results demonstrate that, as compared to the conventional passive suspension, the PALS has a promising potential in full-car application, with up to 70% reduction of the chassis vertical acceleration in speed bumps and chassis leveling capability of dealing with up to 4.3 m/s$^2$ lateral acceleration.**

***Index Terms*—Active suspension, structural optimization, chassis attitude leveling, vehicle vibration control, ride comfort.**

## I. Introduction

Active suspensions for road vehicles are widely studied to improve the ride comfort and handling safety since the 1950s. Recently, due to the mature technology development of sensors, actuators and microcontrollers, as well as the compatibility with electric vehicles, active suspensions have attracted sharply increased attention in both academia and industrial OEMs (Original Equipment Manufacturers). Active suspension systems with improved ride comfort, concise mechanical structure, low energy usage and high reliability are continuously pursued by suspension manufacturers: Bose has been the first to work on linear electromagnetic actuators to fully replace conventional spring-dampers [1]; since then, Michelin has proposed in-wheel active systems with a traction and a suspension actuator integrated [2]; Mercedes-Benz has developed hydraulic actuators in series with suspension springs to implement "Magic Body Control", which is capable of reducing the variation of the chassis roll angle by up to 2.65 degrees in a cornering [3]; air suspensions, the stiffness of which is electronically controlled by pneumatic pump-valve systems, have been developed and widely adopted in the past decade, with the representative examples being the air suspension system technology of AIRMATIC developed by Mercedes-Benz in 2012 [4] and "Smart Air Suspension" developed by Tesla Model S in 2014 [5]; moreover, to enable road preview technology and further fulfill the potential of active suspensions (in terms of ride comfort and road holding improvement), advanced cameras are equipped in some vehicles (*e.g.*, the eROT active suspension system proposed by Audi and installed in Audi A8 in 2017 [6]) to collect the road information ahead. In contrast, academic study on active suspensions emphasizes control strategies design and experimental validations, with $H_\infty$ control [7]-[9] and model predictive control [10]-[11] extensively applied for the chassis vibration reduction, sliding mode control widely adopted for the chassis attitude leveling [12]-[14], and active braking/steering systems incorporated and coordinated with active suspension control systems to further improve vehicle safety [15]-[16].

Recently, a novel mechatronic suspension, the Parallel Active Link Suspension (PALS), has been conceptually proposed in a quarter car setting in [17], [18] and physically implemented in a quarter car test rig in [17], [19], with initial results showing promising prospects. As shown in Fig. 1, a rocker-pushrod assembly ('K-J-F') is introduced in parallel with the conventional spring-damper unit. The active element, the rocker ('K-J'), which is driven by a rotary actuator (*i.e.* the assembly of a servomotor and a gearbox), delivers a torque ($T_{RC}$) acting from the chassis onto the lower wishbone and improving the vehicle suspension performance. It is worth noting that in the PALS physical implementation of [17], [19] shown in Fig. 1-(a), point 'F' is aligned with 'E' due to manufacturing and assembly feasibility. As compared to conventional passive suspensions, the PALS benefits road vehicles with functions of: i) chassis attitude control, and ii) ride comfort and road holding improvement at their frequencies of interests. As compared to other existing active suspensions, the

Manuscript received [month] [date], [year]. This work was supported in part by the U.K. Engineering and Physical Sciences Research Council under Grant Grant EP/N025954/1, and in part by Imperial Innovations.

M. Yu is with the Department of Electrical and Electronic Engineering and the Department of Mechanical Engineering, Imperial College London, SW7 2AZ London, U.K. (e-mail: m.yu14@imperial.ac.uk).

S. A. Evangelou is with the Department of Electrical and Electronic Engineering, Imperial College London, London SW7 2AZ, U.K. (e-mail: s.evangelou@imperial.ac.uk).

D. Dini is with the Department of Mechanical Engineering, Imperial College London, London SW7 2AZ, U.K. (e-mail: d.dini@imperial.ac.uk).

PALS features: i) negligible unsprung mass increment, with the actuation and transmission mechanisms attached onto the chassis, ii) small sprung mass increment, with the active links geometrically optimized to efficiently influence the vertical tire force increment ($\Delta F_{tz}$), iii) structural simplification with the conventional anti-roll bar replaced and its functionality encompassed by these active links at each corner of the chassis, iv) mature and compact technology employment of rotary electromagnetic actuators, and v) fail-safe characteristics in any case of power or actuation failure. It is worth noting that the PALS is inspired and proposed on the basis of the limitation of its "brother" mechatronic suspension, the Series Active Variable Geometry Suspension (SAVGS [20]-[22]), which: i) is complementary to the PALS with the same functions over passive suspensions and the same advantages over other existing active/semi-active suspensions, as mentioned previously, but advantageous for application to different vehicle categories than the PALS, ii) due to its 'series' active-link/spring-damper configuration is deemed to be especially suitable for a GT car with light to medium chassis weight and stiff suspension springs, and iii) demands much larger torque and power from a link-driving actuator when applied to a heavy car such as a SUV. In contrast, the parallel-link-configured PALS can deal with a heavier chassis weight suspended by less stiff springs with lower actuator requirements and power consumption, thus a SUV is selected for numerical investigation in the present work with the PALS.

To further investigate the potential of the PALS in full car application, this paper expands the investigation of the PALS from the quarter car paradigm to a full car paradigm that involves significantly more complex and interacting dynamics. The paper mainly synthesizes a frequency-dependent multi-objective control scheme to fully release the PALS functions at full-car level, and realistic results are presented through numerical simulations with a developed high-fidelity nonlinear model and a group of ISO road events. The main contributions are summarized as follows:

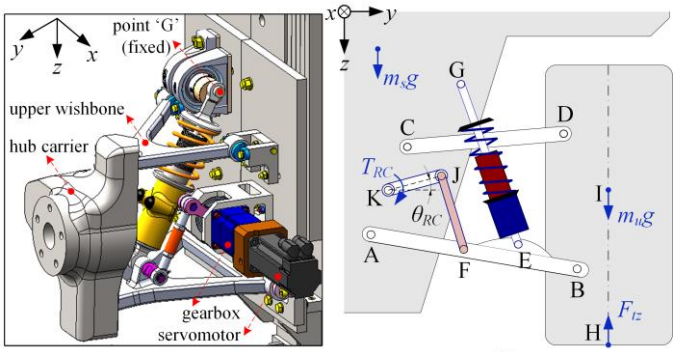


Fig. 1. (a) Physical implementations and (b) principle schematics of the Parallel Active Link Suspension (PALS) in a quarter car with double wishbone suspension [17]. 'A-B' and 'C-D' are the upper- and lower-wishbones respectively, 'G-E' is the spring-damper unit, 'K-J' is the rocker and 'J-F' is the pushrod. $m_s$ and $m_u$ are the sprung and unsprung masses respectively, $F_{tz}$ and $F_{ty}$ are the vertical and lateral tire forces respectively, $\theta_{LW}$ is the angle of the lower wishbone with respect to the horizontal plane, and $T_{RC}$ and $\theta_{RC}$ are respectively the rocker torque and angle, which are controlled by attached rotary servomotor.

a) a general optimization procedure for the rocker-pushrod assembly to maximize the rocker torque propagation to the vertical tire force increment and thereby to maximize the PALS capability of suspension performance improvement;
b) development of a group of mathematical models for the PALS-retrofitted full car to enable numerical analysis and control synthesis, including a nonlinear multi-body model and a linear-equivalent model;
c) control strategies design for the PALS-retrofitted full car: 1) an $H_\infty$ based vehicle vibration control scheme (denoted "PALS-Hinf"), which aims to reach the PALS's maximum capability in terms of ride comfort and road holding improvement at higher frequencies; and 2) a frequency-dependent multi-objective control scheme (denoted "PALS-hybrid"), which effectively and smoothly combines an existing PID based chassis attitude control scheme (denoted "PALS-PID", as synthesized in the conference paper [18] to reach the PALS's maximum capability in terms of chassis leveling and stabilization at lower frequencies) and the proposed "PALS-Hinf" to enable all PALS functions at their frequencies of interest;
d) numerical simulations with the developed nonlinear multi-body model of the PALS-retrofitted full car; the results of suspension performance-related objectives and the energy usage are mainly discussed to evaluate the potential of the PALS solution as well as the robustness of the proposed control strategies.

The rest of this paper is organized as follows. Section II starts with a general optimization for the PALS structure followed by the development of a group of full-car mathematical models to be used for simulation, analysis and control. Section III mainly synthesizes a frequency-dependent multi-objective PALS control strategy for the full-car. Section IV performs numerical simulations and comparisons with a series of ISO-defined road events. Conclusions are finally drawn in Section V.

## II. Mathematical Models and Parameters

In this section, the geometric arrangement and the actuation gearbox ratio of the rocker-pushrod assembly in the PALS are optimized, before developing a set of mathematical models for the PALS-retrofitted full car, including: 1) a nonlinear multi-body model that aims to accurately describe the vehicle dynamics response to different road events in a numerical simulation environment, and 2) a linear equivalent model that enables linear $H_\infty$ control synthesis.

### A. Optimization of Rocker-Pushrod Assembly

In the previous quarter car experimental study for the PALS in [17], the rocker-pushrod has been geometrically optimized while the selection of the actuation transmission ratio compromised to an off-the-shelf 40:1 gearbox. In this subsection, the optimization procedure for the rocker-pushrod assembly is further expanded and generalized by taking the gear ratio selection (within a series of discrete values provided by manuals) into account, inevitably leading to a more complex optimization problem, described as follows.

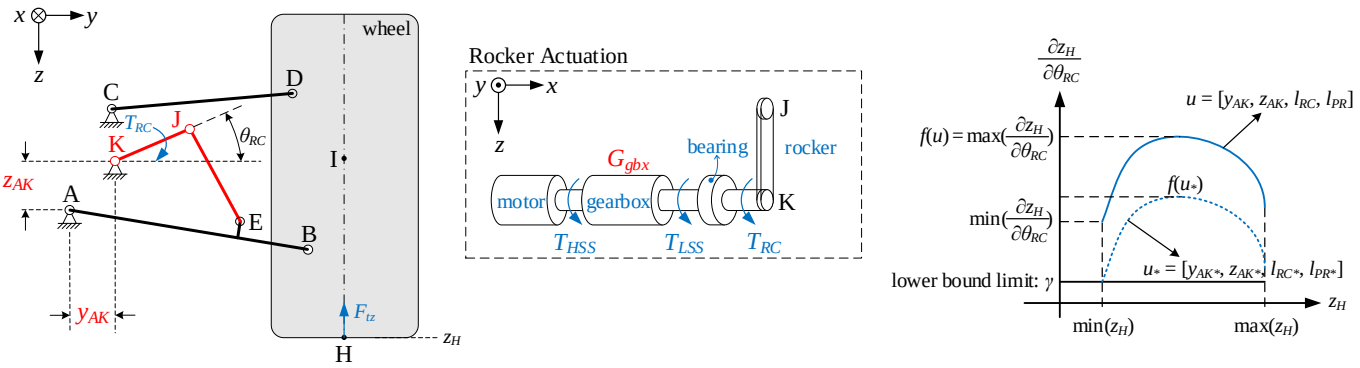


Fig. 2. Equivalent planar linkage of the rocker-pushrod assembly (left), schematic of the rocker actuation package (middle), and illustration of the cost function $f(u)$ with a general vector $u$, and the optimized results of $f(u_*)$ and $u_*$ in the plot of $\frac{\partial z_H}{\partial \theta_{RC}}$ against $z_H$ (right). "HSS" and "LSS" respectively denote the high-speed-shaft and the low-speed-shaft ends of the gearbox. The rocker torque equals the LSS torque (*i.e.*, $T_{RC} = T_{LSS}$), as the transmission backlash [19], [23] between them is ignored in the present work. Parameters to be determined include the geometric variables of $y_{AK}$, $z_{AK}$, $l_{RC} = \overline{KJ}$ and $l_{PR} = \overline{JE}$, and the discrete value of the gearbox ratio, $G_{gbx}$, as highlighted in red.

### *1) Assumptions*

a) In order to physically implement the PALS concept in a real car, the lower end of the pushrod (point 'F' in Fig. 1-b)) is aligned with the bottom joint of the spring-damper (point 'E').

b) The performance improvement by the PALS increases with the rated torque of a selected servomotor. In order to perform a potential comparison between the PALS and the SAVGS in the full car application and to indicate their advantageous vehicle categories (full comparison results are not shown in the present work), the same rotary servomotors that have been adopted in the SAVGS in previous work [20], [21] are selected once again to drive the rocker in the PALS, with Wittenstein TPM series [25] applied in a SUV. Thus, the total mass increment brought about by the SAVGS and the PALS systems is essentially the same and becoming the comparison basis. Therefore, the servomotor-related parameters, including the maximum velocity, $\max(\omega_{HSS})$, and the peak torque, $T_{HSS}^{peak}$ (in the high-speed-shaft, which is connected to the gearbox, as shown in Fig. 2-middle), are fixed as constant values.

With the above assumptions a)-b), the variables to be determined in the rocker-pushrod assembly design include the position of 'K', $[y_{AK}\ z_{AK}]$, the length of rocker, $l_{RC}$, the length of pushrod, $l_{PR}$, and the discrete value of the gearbox ratio, $G_{gbx}$, as highlighted in red in Fig. 2-left) and -middle).

### *2) Cost Functions*

The optimization of the rocker-pushrod assembly aims to maximize the rocker torque ($T_{RC}$) propagation onto the vertical tire force increment ($\Delta F_{tz}$), which is necessary for the maximum potential of the PALS capability in terms of chassis attitude/vibration control and road holding improvement. (The symbol "Δ" in the present work refers to the increment of a variable with respect to its static equilibrium value, where the vehicle is under gravity, at zero forward speed, and none of the system external inputs in the nonlinear model are applied). Theoretically, the maximization should be shown throughout the possible suspension stroke, *i.e.* the $z$-coordinate of the point 'H', $z_H \in [\min(z_H), \max(z_H)]$. However, in practice the geometric configuration at around the nominal position (*i.e.*, $z_H$ = 0 m), where the suspension mostly operates, is considered to be most sensitive to the overall suspension performance, instead of an integral of $\Delta F_{tz}$ from $\min(z_H)$ to $\max(z_H)$.

Assuming that the sprung mass is fixed and applying the virtual work principle to the group of the rocker-pushrod assembly, the lower wishbone and the road wheel, yields:

$$T_{RC}\delta\theta_{RC} = \Delta F_{tz}\delta z_H. \tag{1}$$

where $\theta_{RC}$ is the rocker angle (as defined in Fig. 1 caption).

The maximum achievable vertical tire force increment (for the maximum possible $T_{RC}$) is therefore given by:

$$\max(\Delta F_{tz}) = T_{RC}^{peak} / \frac{\partial z_H}{\partial \theta_{RC}}, \tag{2}$$

where $T_{RC}^{peak}$ is a constant value throughout the suspension stroke and is only determined by the characteristics of the selected gearbox and the servomotor:

$$T_{RC}^{peak} = \min[T_{HSS}^{peak} \cdot G_{gbx} \cdot \eta_{gbx}, T_{LSS}^{peak}], \tag{3}$$

where $T_{HSS}^{peak}$ is the peak torque of servomotor HSS and can be found in the servomotor manual in [25], while $T_{LSS}^{peak}$ and $\eta_{gbx}$ are the peak torque of the gearbox LSS (the output shaft, see Fig. 2-middle) and the gearbox transmission efficiency respectively, both with indicated in the gearbox manual in [26].

The best performance is realized by finding, via the selection of geometric variables of the rocker-pushrod assembly, the greatest lower bound of $\max(\Delta F_{tz})$ throughout the suspension stroke $z_H \in [\min(z_H), \max(z_H)]$, which is given by:

$$\inf_{z_H \in [\min(z_H), \max(z_H)]}(\max(\Delta F_{tz})) = \frac{T_{RC}^{peak}}{\sup_{z_H \in [\min(z_H), \max(z_H)]}\left(\frac{\partial z_H}{\partial \theta_{RC}}\right)}. \tag{4}$$

Thus, $\sup_{z_H \in [\min(z_H), \max(z_H)]}\left(\frac{\partial z_H}{\partial \theta_{RC}}\right)$, which is the least upper bound of $\frac{\partial z_H}{\partial \theta_{RC}}$ throughout the suspension stroke, should be found for a selection of geometric variables of the rocker-pushrod assembly. Therefore, the cost function to be minimized is defined as:

$$f(u) = \max\left(\frac{\partial z_H}{\partial \theta_{RC}}\right), \forall z_H \in [\min(z_H), \max(z_H)], \tag{5}$$

where $u = [y_{AK}\ z_{AK}\ l_{RC}\ l_{PR}]$ include the geometric variables to be determined. For a specific input $u = u_1$, the returned value

of $f(u_1)$ is the maximum value of $\frac{\partial z_H}{\partial \theta_{RC}}$ with $z_H$ swept in the range of $[\min(z_H), \max(z_H)]$. This cost function is used to find an optimal $u = u_*$ with a minimum value of $f(u = u_*)$ (*i.e.*, the least upper bound of $\frac{\partial z_H}{\partial \theta_{RC}}$, as illustrated in Fig. 2-right), such that the rocker torque ($T_{RC}$) influence to the vertical tire force increment ($\Delta F_{tz}$) can be maximized, as indicated by (2).

*3) Constraints*

Primary constraints for the PALS geometry design in a quarter-car physical implementation, as proposed in [17], need to be taken into account and should not be violated in any case, including i) geometry constraints, ii) space constraints, and iii) the velocity constraint of the rotary actuator: $\max(\omega_{HSS}) = G_{gbx} \cdot \max(\omega_{RC})$, further written as:

$$\frac{\partial z_H}{\partial \theta_{RC}} = \frac{\dot{l_s}}{\omega_{RC}} \Rightarrow \left|\frac{\partial z_H}{\partial \theta_{RC}}\right| \geq \frac{G_{gbx} \cdot |\dot{l_s}|}{\max(\omega_{HSS})}, \quad \forall z_H \in [\min(z_H), \max(z_H)], \tag{6}$$

where $\Delta l_s$ is the suspension deflection increment ($\Delta l_s = z_H$ in this case as the sprung mass is assumed to be fixed). Equation (6) should be satisfied in any case, thus the lower bound limit of $\frac{\partial z_H}{\partial \theta_{RC}}$, denoted as $\gamma$ (and illustrated in Fig. 2-right), can be derived:

$$\min\left(\frac{\partial z_H}{\partial \theta_{RC}}\right) \geq \gamma = \frac{G_{gbx} \cdot \max|\dot{l_s}|}{\max(\omega_{HSS})}, \quad \forall z_H \in [\min(z_H), \max(z_H)], \tag{7}$$

where the maximum suspension deflection rate, $\max|\dot{l_s}|$, is a constant that can be approximated through numerical simulation with a "sudden drop" road event (2.40 m/s for a SUV). Therefore, $\gamma$ is a constant for a given value of $G_{gbx}$.

*4) Optimization with Matlab Function fmincon*

With the cost function $f(u)$ given in (5) and the constraints stated above, the Matlab function *fmincon* is employed to find the optimal design variables, $u_*$. For each discrete value of $G_{gbx}$, the corresponding optimization results of $u_* = [y_{AK*}\ z_{AK*}\ l_{RC*}\ l_{PR*}]$ can be returned. Together with $T_{RC}^{peak}$ calculated in (3), a 2-D plot of $\max(\Delta F_{tz})$ against $z_H$ can be produced according to (2). Furthermore, with a series of $G_{gbx}$ values swept and tested, a 3-D plot of $\max(\Delta F_{tz})$ against $z_H$ and $G_{gbx}$ is obtained.

An example of the optimization results for the rear axle in a PALS-retrofitted SUV (the parameters of which are found in Table I in the Appendix) are shown in Fig. 3-left, with the available values of $G_{gbx}$ being [4 5 7 10 16 20 25 28 35 40 50 70 100]. Despite a larger value of $G_{gbx}$ increases $T_{RC}^{peak}$, it does not proportionally contribute to the final objective of $\max(\Delta F_{tz})$, as shown in Fig. 3-middle. This is due to the fact that a larger value of $G_{gbx}$ also increases the lower bound limit $\gamma$, as indicated by (7), and thereby affects the optimization results by lifting the curve of $\frac{\partial z_H}{\partial \theta_{RC}}$ against $z_H$ (*i.e.*, the blue dotted curve illustrated in Fig. 2-right).

Finally, the optimal gearbox ratio of $G_{gbx*} = 20$ is selected as it provides the maximum value of $\max(\Delta F_{tz})$ especially around the nominal position ($z_H$ = 0 m), where the suspension mostly operates. The corresponding optimal geometric arrangement of the rocker-pushrod assembly is $u_* = [y_{AK*}\ z_{AK*}\ l_{RC*}\ l_{PR*}]$ = [59.5 mm -150.6mm 63.5mm 194.4mm], and $\max(\Delta F_{tz})$ ranges [1300N, 2100N] within the suspension stroke $z_H \in$ [-120mm, +110mm], see Fig. 3-right.

## B. Nonlinear Multi-Body Models and Parameters

The "backbone" nonlinear multi-body model of the original vehicle has been developed in *AutoSim* [20], [24], with a 6 degree of freedom (DOF) chassis, spinning wheels, powertrain elements (internal combustion engine, transmission gearbox, propeller shaft and differential mechanism), pinion-rack steering system, braking system, passive suspension assemblies and wheel tire force and moment systems mainly included. The reader is referred to [20] for the full details of this model.

In this work, the nonlinear model of the PALS [17], incorporating a rocker-pushrod mechanical assembly and a Permanent Magnet Synchronous Motor (PMSM) actuation, is integrated at each corner of the chassis in the "backbone" model to establish a PALS-retrofitted full car. The rocker-pushrod assembly at each corner of the chassis is optimized by following the procedures in Subsection II.A. It is worth noting that the backlash between the LSS and the rocker is excluded in the nonlinear model in this paper, as the backlash level primarily depends on the precision of the key-keyway manufacture and assembly [19], [23], therefore $T_{RC} = T_{LSS}$. Additionally, an independent power supply system, which comprises DC batteries and DC/AC inverters (or low-DC to high-DC converters, depending on the selected servo drive power source), feeds the actuator servo drive at each corner to control its corresponding rocker. The electrical energy flow of the ove-

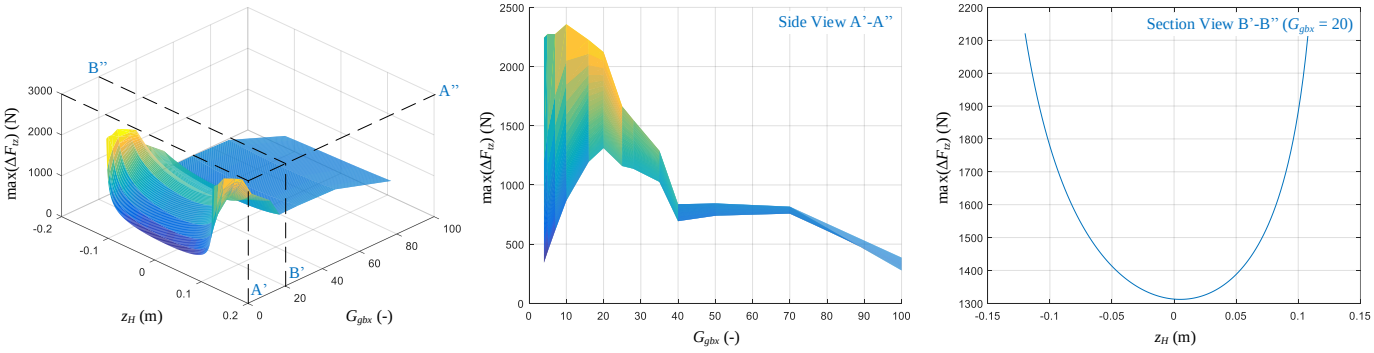


Fig. 3. Optimization results for the rocker-pushrod assembly in the rear axle of a PALS-retrofitted SUV (plots from left to right): 3-D plot of $\max(\Delta F_{tz})$ against $G_{gbx}$ and $z_H$; side view of $\max(\Delta F_{tz})$ against $G_{gbx}$; and section view of $\max(\Delta F_{tz})$ against $z_H$, with $G_{gbx}$ = 20.

rall PALS system in the full car originates from DC batteries, through DC/AC inverters (or DC/DC converters), the servo drives, and terminates at the PMSMs.

Overall, the nonlinear multi-body model of the PALS-retrofitted full car has 17 multi-body degrees of freedom, 115 dynamic states (34 states corresponding to the multi-body freedoms and 81 auxiliary states additionally introduced to model various additional mechanical/electrical components and control modules, such as the engine gearbox dynamics, the dynamics of the three phase currents in the PMSMs driving the PALS rockers, the closed-loop longitudinal and lateral controls (virtual drivers) for following driving maneuvers, the PMSM actuator control loops, and so on). This high-fidelity model enables accurate and realistic assessment on the PALS performance. In terms of the user end, this model provides over 600 output variables for a comprehensive vehicle condition monitoring and has external inputs of i) the disturbance inputs of vertical velocity of the road wheel at the road surface contact point at each of the four wheels, which define the road unevenness, ii) the control input of the reference position of the steering column, iii) the control input of reference position of the braking pedal, which is assumed to be proportional to the braking torque, iv) the control input of the reference position of the gas pedal, which is simplified to be proportional to the produced engine torque, and v) the control inputs of the reference rocker torque in the PALS at each corner of the chassis. The closed-loop longitudinal control that coordinates the position of the gas and braking pedals, and closed-loop lateral control that manipulates the position of the steering column, similarly to [20], [21], are synthesized based on PID algorithms to implement ISO driving maneuvers. The main parameters of the PALS-retrofitted full car are listed in Table I in the Appendix.

### C. Control-Oriented Linear Equivalent Model

To enable linear control synthesis, a linear equivalent model of the PALS-retrofitted full car (a schematic of which is shown in Fig. 4) is mathematically derived, with the nonlinearity of the suspension geometry extracted and compensated. A linear equivalent model of a quarter-car that has been derived in [17] is used as a basis for somewhat more complex derivation here.

The basic assumptions for developing the linear equivalent full car model are as follows: 1) the translational movement of CMC (center of mass of chassis) in both longitudinal and lateral directions, as well as the yaw rotation of the chassis, are restricted; 2) the external inputs of disturbances include the vertical road displacement at each wheel ($^{i}z_r$) and equivalent roll and pitch torques ($T_r$ and $T_p$) due to the load transfer effect under cornering and driving/braking respectively; and 3) the vertical position at each corner of the chassis is linearized and approximated as:

$$\begin{aligned} {}^{1}z_s &= z_{CMC} - b_f\theta - \tfrac{t_f}{2}\phi,\ {}^{2}z_s = z_{CMC} - b_f\theta + \tfrac{t_f}{2}\phi, \\ {}^{3}z_s &= z_{CMC} + b_r\theta - \tfrac{t_r}{2}\phi,\ {}^{4}z_s = z_{CMC} + b_r\theta + \tfrac{t_r}{2}\phi. \end{aligned} \tag{8}$$

The vertical velocity and vertical acceleration at each corner of the chassis are the first and second time derivatives of $^{i}z_s$ respectively.

Based on fundamental physics arguments, the following

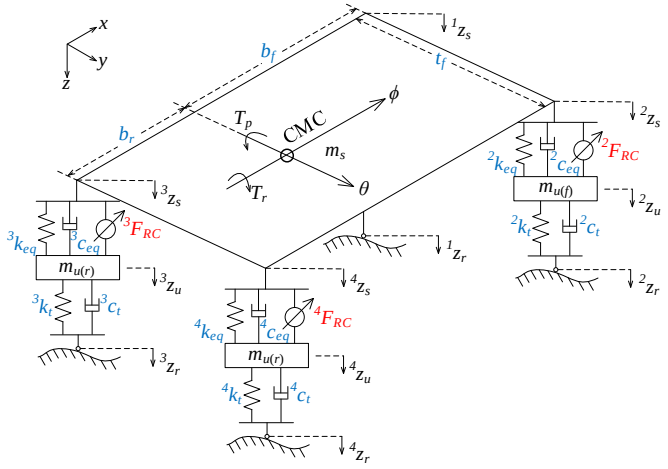


Fig. 4. Schematic of linear equivalent model of the PALS-retrofitted full car. $\theta$ and $\phi$ are the pitch and roll angles of the chassis respectively, $t_f$ and $t_r$ are the front and rear track width, $b_f$ and $b_r$ are the front and rear parts of the wheelbase as divided by CMC, $^{i}z_s$, $^{i}z_u$ and $^{i}z_r$ are the vertical coordinates of points 'G', 'I' and 'H' (see Fig. 1-b)) respectively at each corner of the vehicle. The left-superscript $i$ = 1, 2, 3 and 4 corresponds to the corner number of front-left, front-right, rear-left and rear-right respectively.

three steps are followed to obtain the equivalence between the linear and nonlinear full car models, thus leading to the derivation of the novel linear equivalent full-car model. Firstly, the equivalent spring-damper force at each corner is:

$$^{i}\Delta F_{SD}^{(eq)} = {}^{i}k_{eq} \cdot {}^{i}\Delta l_s + {}^{i}c_{eq} \cdot {}^{i}\dot{l}_s, \tag{9}$$

where $^{i}l_s = {}^{i}z_u - {}^{i}z_s$ is the suspension deflection, and the spring stiffness $^{i}k_{eq}$ (given the equivalence of vertical force acting onto the chassis) and damping coefficient $^{i}c_{eq}$ (given the equivalence of energy dissipated) are solely dependent on the original passive suspension geometric arrangement, satisfying:

$$\begin{aligned} {}^{i}k_{eq} &= \frac{d\,{}^{i}F_S^{(eq)}}{d\,{}^{i}l_s} = \frac{d\left({}^{i}F_S \frac{d\,{}^{i}l_{SD}}{d\,{}^{i}l_s}\right)}{d\,{}^{i}l_s}, \\ {}^{i}c_{eq} &= \left(\frac{d\,{}^{i}l_{SD}}{d\,{}^{i}l_s}\right)^2 {}^{i}c_{SD}, \end{aligned} \tag{10}$$

where $^{i}F_S$ is the actual spring force while $^{i}F_S^{(eq)}$ is the linear equivalent spring force that is acting vertically between the chassis and the road wheel, $^{i}l_{SD}$ is the length of the spring damper unit, and $^{i}c_{SD}$ is the damping coefficient of the damper. In order to obtain a linear system that is independent of the suspension deflection, $^{i}k_{eq}$ and $^{i}c_{eq}$, both of which vary moderately with the suspension deflection increment $^{i}\Delta l_s$, are further approximated to constant values at their static equilibrium state (where none of the system external inputs are applied); see a similar argument for the quarter car derivation in [17].

The second equivalence step recognizes that the linear equivalent actuator at each corner has the same power output as the actual rotary actuator, with the produced linear equivalent actuation force $^{i}F_{RC}$ satisfying:

$$^{i}T_{RC}\delta\,{}^{i}\theta_{RC} - {}^{i}F_{RC}\delta\,{}^{i}l_s = 0. \tag{11}$$

Transformation functions between $^{i}F_{RC}$ and $^{i}T_{RC}$ at each corner are defined as follows:

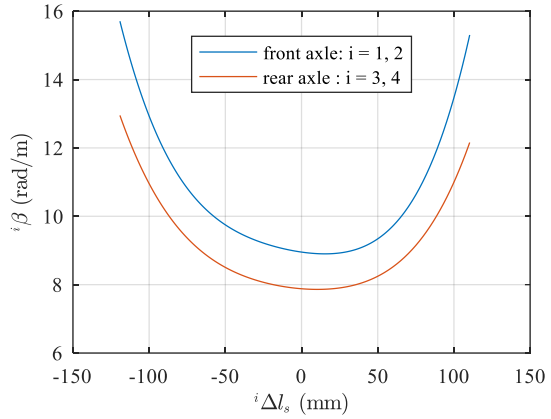


Fig. 5. Variation of transformation functions ($^i\beta$) with respect to the suspension deflection increment ($^i\Delta l_s$) in a PALS-retrofitted SUV.

$$^i\beta = {}^i\beta(^i\Delta l_s) = \frac{^i F_{RC}}{^i T_{RC}} = \frac{\partial {}^i\theta_{RC}}{\partial {}^i l_s}, \tag{12}$$

which can be derived through the suspension geometry variation against the suspension deflection increment ($^i\Delta l_s$), as plotted in Fig. 5 (where the parameters of a PALS- retrofitted SUV in Table I in the Appendix are employed). Transformation functions $^i\beta$ not only bridge the linear equivalent model and the nonlinear multi-body model, but also incorporate and compensate the varied geometry nonlinearity throughout the suspension stroke.

The third and final equivalence step involves the integration of the equivalent spring-damper and actuator at each corner of the chassis, to obtain the full-car linear equivalent dynamics with the load transfer (due to braking/accelerating/cornering) effectively coupled. The vertical tire force at each road wheel is given as:

$$^i\Delta F_{tz} = {}^i k_t \cdot {}^i\Delta l_t + {}^i c_t \cdot {}^i\dot{l}_t, \tag{13}$$

where $^i l_t = {}^i z_r - {}^i z_u$ is the tire deflection of the road wheel at each corner, $^i k_t$ and $^i c_t$ are the tire's radial stiffness and damping respectively. Applying Newton's second law to the CMC, yields:

$$m_s \ddot{z}_{CMC} = \sum_{i=1}^{4} \left( {}^i\Delta F_{SD}^{(eq)} + {}^i F_{RC} \right). \tag{14}$$

According to the balance of pitching moments:

$$\begin{aligned} I_{yy}\ddot{\theta} = &-\left({}^1\Delta F_{SD}^{(eq)} + {}^1F_{RC}\right)b_f - \left({}^2\Delta F_{SD}^{(eq)} + {}^2F_{RC}\right)b_f \\ &+\left({}^3\Delta F_{SD}^{(eq)} + {}^3F_{RC}\right)b_r + \left({}^4\Delta F_{SD}^{(eq)} + {}^4F_{RC}\right)b_r + T_p, \end{aligned} \tag{15}$$

and of rolling moments:

$$\begin{aligned} I_{xx}\ddot{\phi} = &-\left({}^1\Delta F_{SD}^{(eq)} + {}^1F_{RC}\right)\frac{t_f}{2} + \left({}^2\Delta F_{SD}^{(eq)} + {}^2F_{RC}\right)\frac{t_f}{2} \\ &-\left({}^3\Delta F_{SD}^{(eq)} + {}^3F_{RC}\right)\frac{t_r}{2} + \left({}^4\Delta F_{SD}^{(eq)} + {}^4F_{RC}\right)\frac{t_r}{2} + T_r. \end{aligned} \tag{16}$$

Applying Newton's second law to the unsprung mass at each corner, yields:

$$^i m_u {}^i\ddot{z}_u = {}^i\Delta F_{tz} - {}^i\Delta F_{SD}^{(eq)} - {}^i F_{RC}. \tag{17}$$

With the suspension parameters of $^i k_{eq}$ and $^i c_{eq}$ linearized in a quarter car (see (9)-(10)) and the suspension dynamics coupled in a full car (see (13)-(17)), the state-space representation of the linear equivalent model of the PALS-retrofitted full car can be completely constructed. The state vector $\hat{x}$, the performance outputs $\hat{y}$ and exogenous inputs $\hat{u}$ are as follows:

$$\begin{aligned} \hat{x}^T &= \left[\dot{z}_{CMC} \quad \dot{\theta} \quad \dot{\phi} \quad {}^i\dot{z}_u \quad {}^i\Delta l_s \quad {}^i\Delta l_t\right]_{1\times 15}, \\ \hat{y}^T &= \left[\ddot{z}_{CMC} \quad \ddot{\theta} \quad \ddot{\phi} \quad {}^i\Delta l_s \quad {}^i\Delta l_t\right]_{1\times 11}, \\ \hat{u}^T &= \left[{}^i\dot{z}_r \quad T_p \quad T_r \quad {}^i F_{RC}\right]_{1\times 10}. \end{aligned} \tag{18}$$

## III. Control Strategies Development

This section presents three different control strategies for the PALS-retrofitted SUV (the parameters of which are given in Table I in the Appendix), as follows:

1) An existing PID based chassis attitude control scheme ("PALS-PID"), which has been synthesized in [18] to achieve the PALS's maximum capability in terms of chassis leveling or stabilization at low frequencies;

2) A novel $H_\infty$ based vehicle vibration control scheme ("PALS-Hinf"), which aims to obtain the PALS's maximum capability in terms of ride comfort and road holding improvement at higher frequencies;

3) A novel frequency-dependent multi-objective control scheme ("PALS-hybrid"), which combines effectively and seamlessly "PALS-PID" and "PALS-Hinf" to enable all PALS functions at their frequencies of interests: the tracking control for the chassis leveling at 0-1 Hz, the attenuation control for the vehicle vibration at 1-8 Hz, and the control gains penalization at frequencies above 10 Hz).

### A. PID Based Chassis Attitude Leveling ("PALS-PID")

To achieve desirable chassis attitude and driving dynamics for the PALS-retrofitted full car (for example, lowering the front end of the chassis at high-speed driving for better aerodynamics, leveling the chassis at braking and cornering events, and lifting one side of the chassis to possibly avoid a car clash), a multi-objective PID control scheme is developed in [18]. This scheme is adopted in the present work and summarized here, with a focus on the minimization of the pitch and roll angle variations (*i.e.*, the chassis leveling). The reference rocker torques at each corner ($^i T_{RC*}$) are the manipulated control variables, which are given in [18] and as follows.

The contributions to the reference rocker torque increments at each corner for the pitch angle minimization are:

$$\begin{aligned} {}^1\Delta T_{RC*}^{(1)} &= {}^2\Delta T_{RC*}^{(1)} = -K_{p,f}^{(1)}\dot{\theta} - K_{i,f}^{(1)}\theta - K_{d,f}^{(1)}\ddot{\theta}, \\ {}^3\Delta T_{RC*}^{(1)} &= {}^4\Delta T_{RC*}^{(1)} = +K_{p,r}^{(1)}\dot{\theta} + K_{i,r}^{(1)}\theta + K_{d,r}^{(1)}\ddot{\theta}, \end{aligned} \tag{19}$$

and the contributions to the reference rocker torque increments for the roll angle minimization are:

$$\begin{aligned} {}^1\Delta T_{RC*}^{(2)} &= -{}^2\Delta T_{RC*}^{(2)} = -K_{p,f}^{(2)}\dot{\phi} - K_{i,f}^{(2)}\phi - K_{d,f}^{(2)}\ddot{\phi}, \\ {}^3\Delta T_{RC*}^{(2)} &= -{}^4\Delta T_{RC*}^{(2)} = +K_{p,r}^{(2)}\dot{\phi} + K_{i,r}^{(2)}\phi + K_{d,r}^{(2)}\ddot{\phi}, \end{aligned} \tag{20}$$

where the PID tuning parameters in (19) and (20) (using Ziegler–Nichols tuning method) are listed in Table II in the Appendix. As shown in Fig. 6, the reference rocker torque increments are further combined and added to the actual value of rocker torques, $^i T_{RC}$ to produce the overall reference rocker torques:

$$^i T_{RC*} = {}^i T_{RC} + {}^i\Delta T_{RC*}^{(1)} + {}^i\Delta T_{RC*}^{(2)}. \tag{21}$$

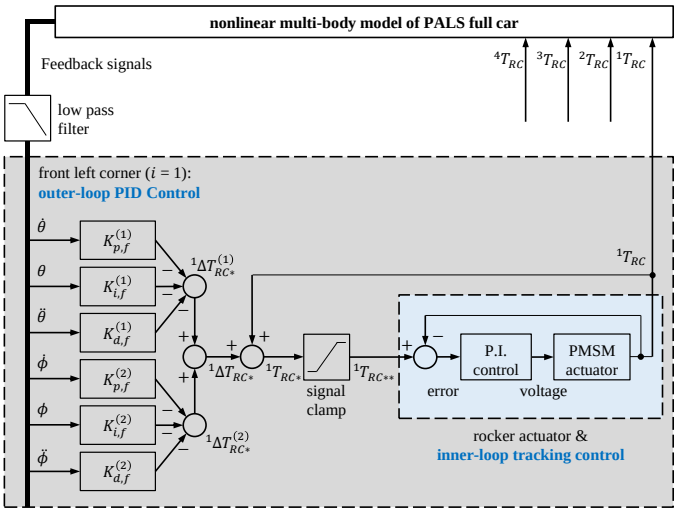


Fig. 6. Implementation of the multi-objective PID control scheme ("PALS-PID") in the nonlinear multi-body model of the PALS-retrofitted full car (built in Subsection II.B). Only the front-left corner ($i$ = 1) case is presented, while the cases of ${}^2T_{RC}$, ${}^3T_{RC}$ and ${}^4T_{RC}$ similarly refer to (19)-(21).

${}^iT_{RC*}$ are further clamped by the peak torque of the rocker ($T_{RC}^{peak}$) before feeding the rotary PMSM actuator at each corner. Moreover, the inner-loop torque tracking control (from ${}^iT_{RC**}$ to ${}^iT_{RC}$) in the PMSM actuator employs the classic $d$-$q$ transformation and zero $d$-axis current control strategy ($i_{d*}$ = 0 A, proposed in [27], not expanded here), such that the three-phase PMSM behaves like a DC equivalent motor, with the produced torque (${}^iT_{RC}$) proportional solely to the $q$-axis current ($i_q$).

It is worth noting that the incremental PID form, as in (19)-(21), is selected in the present work over the typical PID form (for example, $T_{RC*}^{(i)} = K_p^{(i)}\theta + K_i^{(i)}\int\theta + K_d^{(i)}\dot{\theta}$, which also demonstrates similar capability in terms of chassis leveling in numerical simulations of the continuous-time systems). This is mainly to ensure the control performance in practice, where a discrete-time platform would be used, and where an inertial measurement unit (IMU) or other similar sensors are normally deployed in a car to enable measurements of the chassis-related dynamics, including yaw / pitch / roll angles, rates, and accelerations, and longitudinal / lateral / vertical displacements, velocities, and accelerations. These conditioned signals are more suitable to be directly taken as measurements feedback in the control framework in discrete-time systems, as in contrast, any signal integral and derivative in the control loop (that would take place if a typical PID was employed) may result in a delayed response and magnified noise (particularly for low-sampling-rate real-time systems). To deal with this, a state observer (for example, a Kalman Filter) would be needed to reconstruct the required signals. Therefore, the incremental PID form, with the inputs of the pitch/roll angles, rates, and accelerations (directly provided by an IMU sensor) and the rocker torque (a scaled current signal directly provided by the PMSM), is adopted to implement "PALS-PID".

### *B. $H_\infty$ Based Vehicle Vibration Control Strategy ("PALS-Hinf")*

The $H_\infty$ control technique has been widely utilized in active suspensions to enhance ride comfort and road holding through reducing vehicle vibration, as it aims to attenuate the influence from multiple-external disturbances (*e.g.* the vertical road velocity and the load transfer effect) to multi-objective errors (*e.g.* CMC vertical acceleration and vertical tire force increment at each corner) by synthesizing a control solution with robustness and performance guaranteed. Mathematically, the $H_\infty$ control is looking to find an optimal controller $\widehat{K}$ that minimizes the linear fractional transformation $F_\ell(\hat{P},\widehat{K})$ according to the definition of the $H_\infty$ norm:

$$\left\|F_\ell(\hat{P},\widehat{K})\right\|_\infty = \sup\bar{\sigma}\left(F_\ell(\hat{P},\widehat{K})(j\omega)\right), \tag{22}$$

where $\hat{P}$ is the system plant, $\bar{\sigma}$ is the maximum singular value of the matrix $F_\ell(\hat{P},\widehat{K})(j\omega)$, and "sup" refers to the least upper-bound.

Fig. 7 shows the $H_\infty$ control configuration with the linear equivalent model of the PALS-retrofitted full car (derived in Subsection II.C). The normalized system disturbance inputs $[{}^id_1 \quad d_2 \quad d_3]_{1\times6}$ are: 1) ${}^id_1$, the vertical road velocity of each wheel, 2) $d_2$, the equivalent pitch torque due to load transfer during braking/acceleration, and 3) $d_3$, the equivalent roll torque caused by load transfer during cornering. The weighted performance objectives $[e_1 \quad e_2 \quad e_3 \quad {}^ie_4 \quad {}^ie_5]_{1\times11}$ to be minimized are: 1) the ride comfort related variables of $e_1$-$e_3$, which are the CMC vertical acceleration and the roll and pitch accelerations, 2) the road holding related variables ${}^ie_4$, which are the vertical tire deflection increment at each corner, and 3) the control effort of the reference rocker torque at each corner ${}^ie_5$, which aims to attenuate control outputs at higher (non-human sensitive) frequencies, as well as to reduce the power usage. The measurements feedback signals $y = [\ddot{z}_{CMC} \quad \ddot{\theta} \quad \ddot{\phi} \quad {}^i\Delta l_s]_{1\times7}$ are selected based on sensors availability. The control manipulated variables $u = [{}^1F_{RC} \quad {}^2F_{RC} \quad {}^3F_{RC} \quad {}^4F_{RC}]_{1\times4}$ are the linear equivalent actuation forces at each corner.

Disturbance weighting functions $[{}^iW_{d1} \quad W_{d2} \quad W_{d3}]_{1\times6}$ are selected as constants corresponding to the respective maximum expected values of the disturbances, which aim to normalize the inputs by removing physical unit discrepancy, as follows:

$$\begin{aligned} {}^iW_{d1} &= \max\left|{}^i\dot{z}_r\right| = 0.25\ m/s, \\ W_{d2} &= \max\left|T_p\right| = 4000\ N\cdot m, \\ W_{d3} &= \max\left|T_r\right| = 4000\ N\cdot m. \end{aligned} \tag{23}$$

$\left[W_{e1} \quad W_{e2} \quad W_{e3} \quad {}^iW_{e4} \quad {}^iW_{eff}\right]_{1\times11}$ are the weighting functions that indicate the importance levels between different output objectives, with the human-sensitive bandwidth for vertical (translational) motion (0.5-8 Hz) and rotational motion (0.5-4 Hz) respected [32]. These weighting functions are tuned and listed as:

$$\begin{aligned} W_{e1} &= \frac{1}{0.04}\frac{1}{\frac{s}{2\pi\cdot10}+1}, W_{e2} = \frac{1}{0.08}\frac{1}{\frac{s}{2\pi\cdot1}+1}, \\ W_{e3} &= \frac{1}{0.08}\frac{1}{\frac{s}{2\pi\cdot1}+1}, {}^iW_{e4} = \frac{1}{0.0045}\frac{1}{\frac{s}{2\pi\cdot5}+1}, \\ {}^iW_{eff} &= \frac{1}{0.002}\frac{\left(\frac{s}{2\pi\cdot10}+1\right)^2}{\left(\frac{s}{2\pi\cdot100}+1\right)^2}, \end{aligned} \tag{24}$$

where the cut-off frequencies are tuned to ensure the corresponding performance objectives are improved at around

their frequencies of interest, and the DC gains are related to the maximum expected values, thus also determining the control aggressiveness.

Bode magnitude diagrams of linear equivalent models of the full car with and without the PALS are plotted in Fig. 8. It can be seen that the synthesized $H_\infty$ control scheme significantly attenuates the propagation from the external disturbances (the road velocity and the load transfer) to the suspension performance objectives (ride comfort related variables of CMC vertical acceleration, pitch and roll accelerations, and road holding related variables of the vertical tire force increment of each wheel) at their frequencies of interest. It is worth noting that the vertical tire force increment ($^i\Delta F_{tz}$), instead of the vertical tire deflection increment ($^i\Delta l_t$), is used to assess the road holding performance in both linear and nonlinear analysis results (later shown in Section IV). This choice is made because the two quantities are very similar (exactly proportional if tire damping is neglected) and can equally be associated with the road holding evaluation, however, in practice $^i\Delta F_{tz}$ is easier to measure than $^i\Delta l_t$ by appropriate sensors.

The linear analysis results indicates the expected suspension performance enhancement by the PALS, while accurate and reliable vehicle dynamics response is provided subsequently by simulations with nonlinear multi-body models. The $H_\infty$ control scheme implementation in the nonlinear model of the PALS-retrofitted full car is shown in Fig. 9. The control outputs $^iF_{RC*}$ are further transformed to $^iT_{RC*}$ by functions $^i\beta$, which are derived in (12) and illustrated in Fig. 5. The inner-loop torque tracking control of the rocker actuator (from $^iT_{RC*}$ to $^iT_{RC}$) is the same as in "PALS-PID", see Subsection III.A.

### *C. Frequency-Dependent Multi-Objective Control Scheme ("PALS-hybrid")*

To enable implementable synchronous control of both low-frequency signal tracking and high-frequency vibration attenuation, a novel frequency-dependent multi-objective control scheme is proposed, with the $H_\infty$ control scheme ("PALS-Hinf" in Subsection III.B) modified to bridge the multi-objective PID control scheme ("PALS-PID" in Subsection III.A), as shown in Fig. 10. Exogenous disturbances of low-frequency reference signals $^iF_{RC*}^{(L)}$ are introduced, and their tracking error ($^iF_{RC*}^{(L)} - {}^iF_{RC}$) is included in the performance

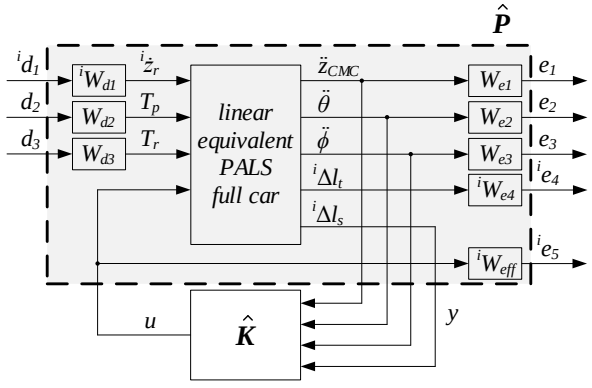


Fig. 7. $H_\infty$ control synthesis framework ("PALS-Hinf") with the linear equivalent model of the PALS-retrofitted full car (derived in Subsection II.C). $\hat{P}$ is the constructed system plant, $\hat{K}$ is the $H_\infty$ controller to be synthesized, $u$ are the manipulated control variables, $d$ are the system disturbance inputs, $e$ are the weighted performance objectives, and $y$ are the measurements feedback.

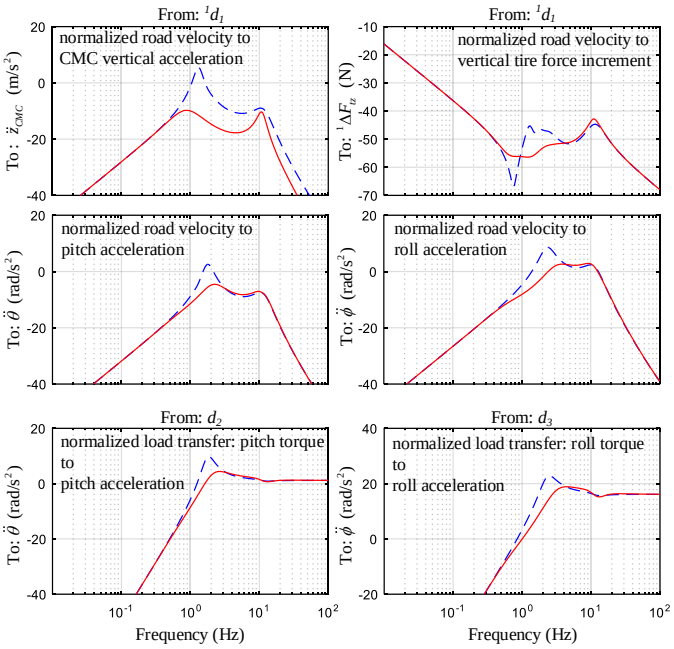


Fig. 8. Magnitude bode diagrams of the full car with the "PALS-Hinf" (red solid line) and without any controllers (*i.e.*, $^iT_{RC}$ = 0 N m, in blue dashed line).

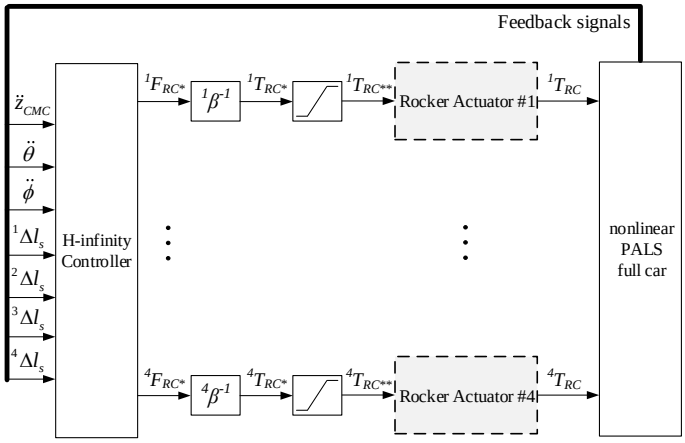


Fig. 9. $H_\infty$ control implementation ("PALS-Hinf") in the nonlinear multi-body model of the PALS-retrofitted full car (built in Subsection II.B).

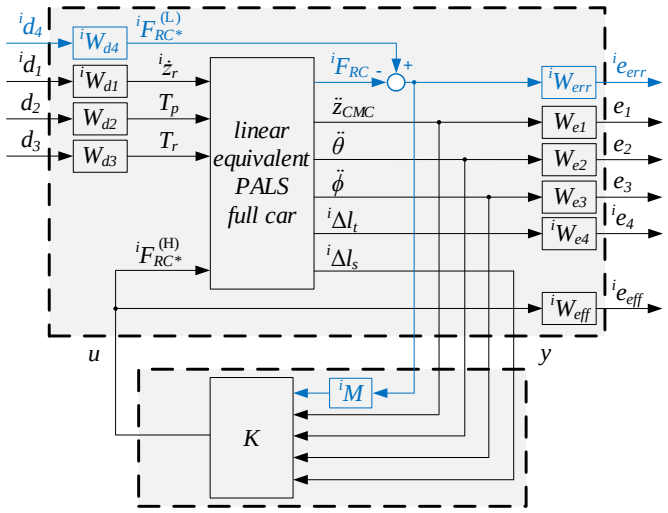


Fig. 10. $H_\infty$ control synthesis framework to enable frequency-dependent multi-objective control ("PALS-hybrid"). All variables correspond to those in Fig. 7, while the changes with respect to Fig. 7 are highlighted in blue.

objective list. To ensure zero tracking error, free integrators shown as block '$^iM$' are added between the tracking errors and the $H_\infty$ controller to be synthesized [28].

The overall tuning of "PALS-hybrid" involves fairly decoupled processes of tuning of the $H_\infty$ and PID parts as follows:

1. $H_\infty$ tuning – stage I: Select the weighting functions $^iW_{d1}$, $W_{d2}$ and $W_{d3}$, $W_{e1}$, $W_{e2}$, $W_{e3}$, $W_{e4}$, $W_{eff}$ by tuning PALS-Hinf (as in (23)-(24) in Section III.B).
2. $H_\infty$ tuning – stage II: The introduced $W_{d4}$ (see Fig. 10) aims to eliminate the unit influence of $^iF_{RC}$, and it is selected as $^iW_{d4} = \max|^iF_{RC}| = 1800$ N. Apply step inputs of low-frequency reference rocker torque signals, $^iT_{RC*}^{(L)}$ (equal to the maximum $^iT_{RC}$ = 273 N·m) in all four corners in the numerical simulation environment with the $H_\infty$ controller synthesized in Fig. 10 implemented with the nonlinear multi-body PALS full car model, as shown in Fig. 11 ("open-loop" system without the PID control part), and select $^iM$ and $^iW_{err}$ as (25)-(26) to exhibit the desirable time response (short rise time and negligible overshoots) for $^iT_{RC}$ tracking performance. Block '$^iM$' incorporates a free integrator and is tuned as:
$$^iM = \frac{\frac{s}{2\pi\cdot 1}+1}{s}. \quad (25)$$
$^iW_{err}$ is to penalize the tracking error of $^iF_{RC*}^{(L)} - {}^iF_{RC}$ at low frequencies, with a first-order transfer function adopted and tuned as:
$$^iW_{err} = \frac{1}{0.35}\frac{1}{\frac{s}{2\pi\cdot 0.001}+1}. \quad (26)$$
3. PID tuning – stage I: Select the initial PID gains by tuning "PALS-PID" as in Section III.A.
4. PID tuning – stage II: With the new $H_\infty$ controller ($K$ and $^iM$ shown in Fig. 10) synthesized, the implementation of the proposed frequency-dependent multi-objective control scheme ("PALS-hybrid") in the PALS-retrofitted full car is shown in Fig. 11. The new $H_\infty$ controller (top-left dashed block) takes effect at high-frequency road events to enhance the ride comfort and the road holding, while the multi-objective PID control (bottom-right dashed block) stabilizes the rocker torque at each corner in low-frequency road events to achieve the desirable chassis attitude. Re-tune the PID gains (starting from the values obtained in PID tuning – stage I) to ensure the "PALS-hybrid" can achieve decent control performance in both the low-frequency chassis leveling and high-frequency vibration attenuation (by observing numerical simulation results with the nonlinear models). The re-tuned gains are listed in Table II in the Appendix. Moreover, functions $^i\beta$ in (12) are utilized again to bridge the rocker torque ($^iT_{RC}$) in the nonlinear multi-body model and the linear actuation force ($^iF_{RC}$) in the linear equivalent model.

### *D. Remarks on Control Tuning*

The complexity of the multiple-input and multiple-output (MIMO) control system of the PALS-retrofitted full car demands considerable effort of tuning work, as the performance objectives can be contradictory to each other at different frequencies, thus a compromise is inevitable. Also, more control objectives are likely to lead to more performance compromise. For the control scheme of "PALS-PID", the rolling and pitching PID parameters can affect the performance of each other objective, as aggressive roll angle minimization means conservative pitch angle minimization, thus the tuning parameters in "PALS-PID" can be categorized as: 1) roll angle focused, 2) pitch angle focused, and 3) a compromised balance of minimization in both roll and pitch angles, which is used in the present work. For the control scheme of "PID-Hinf", an aggressive weighting function to ride comfort likely results in a deterioration in road holding performance (with an increased vertical tire deflection increment at around the unsprung resonant frequency), which occurs in most active suspension systems presented (e.g. in the literature [10]). Thus, the DC gains and cut-off frequencies of weighting functions in "PALS-Hinf" control framework need to be thoroughly tuned by observing the linear analysis results (shown in Fig. 7) as well as the subsequent nonlinear numerical simulation results (shown in Fig. 15 and Fig. 16), ensuring that a decent performance improvement can be seen over the passive suspension at and only at around frequencies of interest; meanwhile, any performance deterioration is minimized to an acceptable level within the frequencies of interest or it occurs outside the frequencies of interest. Similarly, despite the control scheme "PALS-hybrid" is able to simultaneously implement the functions of both "PALS-PID" (low-frequency chassis attitude stabilization) and of "PALS-Hinf" (high-frequency vehicle vibration attenuation), it is enabled by very similar control performance as compared to "PALS-PID" and sacrificed performance as compared to "PALS-Hinf" for its individual functions (however, it should not be forgotten that "PALS-PID" alone is ineffective for the functions of "PALS-Hinf" and vice versa, thus "PALS-hybrid" offers an effective solution for the totality of functions). Nevertheless, by tuning the parameters in "PALS-hybrid", this sacrifice is kept low such that this scheme has close control performance to both "PALS-PID" or "PALS-hybrid" for their individual functions. Overall, all the parameters in the above three control schemes are thoroughly tuned to completely demonstrate their corresponding functions.

To enable more realistic and practical control tuning, further tuning of the proposed control schemes by more sophisticated methods, such as methods involving neural networks and adaptive tuning, is possible and could be considered in future work. However, the further improvement that may be achieved is not expected to be significant.

## IV. Numerical Simulations with Nonlinear Models

With the nonlinear multi-body models built in Subsection II.B and three control strategies developed in Section III, numerical simulations are performed in this section to evaluate the PALS potential in terms of the suspension performance and the power consumption, as well as the robustness of the synthesized controllers.

A group of ISO defined road events are tested, including: a) steady-state cornering, b) step steer, c) braking in a turn, d) speed bump, and e) random road Class A and C. Among them, a), b) and c) are case studies for low-frequency chassis leveling,

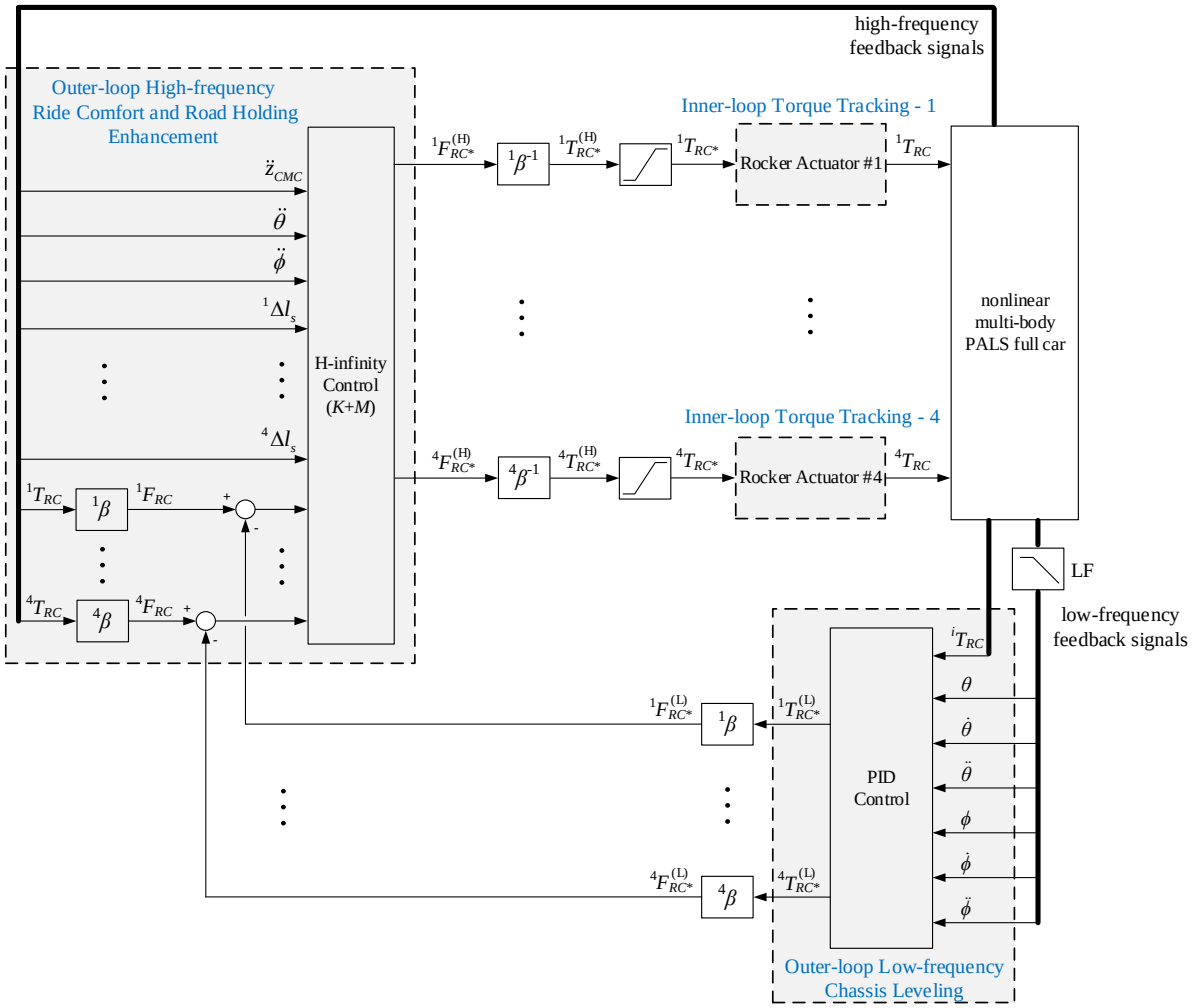


Fig. 11. Implementation of the frequency-dependent multi-objective control scheme ("PALS-hybrid") in the nonlinear model of PALS-retrofitted full car.

thus the control strategies "PALS-PID" and "PALS-hybrid" are applicable, while d) and e) are investigation cases for vehicle vibration control (*i.e.*, the ride comfort and the road holding enhancement) and therefore the control strategies "PALS-Hinf" and "PALS-hybrid" are to be employed.

All numerical simulation results are plotted in Fig. 12-Fig. 16, and are also quantified in Table III in the Appendix.

### A. *Case Study with Steady-state Cornering*

ISO 4138: 2004 details an open-loop test method for recognizing the response of passenger vehicles in steady-state circular driving [28]. Accordingly, in the numerical simulation environment, the nonlinear multi-body model of the PALS-retrofitted full car is driven at a constant longitudinal speed of $v_x$ = 100 km/h, with the angle of the steering wheel linearly increased from 0 to 60 degrees in 400 s.

Fig. 12-1) depicts the variation of the chassis roll angle ($\phi$) against the vehicle lateral acceleration ($a_y$), indicating that "PALS-PID" is capable of fully leveling the chassis during cornering with a lateral acceleration up to 4 m/s$^2$. Despite the output mechanical power of the rocker actuation is small in this steady-state case, the total power consumption in the DC batteries is up to 1.5kW, as shown in Fig. 12-2). Additionally, Fig. 12-3) shows the variation of the rocker torque at each corner, ${}^iT_{RC}$, which saturates at the peak limit of 273 N·m.

The control strategy "PALS-hybrid" presents the same performance as "PALS-PID", as the block '${}^iM$' is capable of zeroing the tracking errors between the ${}^iT_{RC*}^{(L)}$ and ${}^iT_{RC}$ at low-frequency road events. The variation of ${}^iT_{RC}$ in the "PALS-hybrid" case is depicted in Fig. 12-4).

### B. *Case Study with Step Steer*

ISO 7401:2011 defines an open-loop test method to determine the transient response behavior of road vehicles [30]. Accordingly, the PALS-retrofitted full car is again driven at a constant longitudinal speed of $v_x$ = 100 km/h, while the angle of the steering column is linearly increased from 0 to 48.6 deg at a constant rate of 500 deg/s, such that the vehicle stabilizes at a lateral acceleration of $a_y$ = 8 m/s$^2$. The numerical simulation results are shown in Fig. 13, indicating that for the control strategy "PALS-PID": a) the peak roll angle is reduced by 30% as compared to the passive suspension, b) the total power consumption in the DC batteries, $P_{battery}$, has a peak value close to 2.5 kW, and c) and the rocker torque at each corner, ${}^iT_{RC}$, is stabilized at the peak torque value of 273 N·m.

The "PALS-hybrid" presents a control performance that is close to the "PALS-PID" performance, with the chassis roll angle $\phi$ stabilized at the same value of approximately -4 degrees in the end, and with a lower peak power consumption (approximately 1.8 kW). The rocker torque variation with the

control scheme "PALS-hybrid" is shown in Fig. 13-4).

### C. Case Study with Braking in a Turn

ISO 7975:2006 presents an open-loop test method for determining the steady-state circular response of a vehicle that is altered by sudden braking [31]. Accordingly, in the numerical simulation environment, the PALS-retrofitted full car is initially driven at a constant longitudinal speed of $v_x$ = 80 km/h and a path radius of 100 m (which ensures the tested vehicle has a constant lateral acceleration of $a_y$ = 5 m/s$^2$) in 0-5 s, and then brakes to a stop with a constant deceleration of $a_x$ = -5 m/s$^2$ in 5-9.4 s, while keeping the angle of the steering column fixed.

The numerical simulation results are shown in Fig. 14. As it can be seen, as compared to the passive suspension, the "PALS-PID" significantly attenuates the roll angle $\phi$ at the initial cornering stage (0-5 s), from -4˚ to approximately -1.5˚, while in the braking stage (5-9.4 s), the average pitch angle $\theta$ is reduced from -1.5˚ to -0.5˚. Once again, the control strategy "PALS-hybrid" shows a similar performance as compared to "PALS-PID" due to the low frequency nature of the maneuver. The variation of the rocker torque at each corner for "PALS-hybrid" is illustrated in Fig. 14-4).

### D. Case Study with Speed Bump

Speed bumps or humps are common devices in a roadway and are typically approximated as a sinusoidal shape. In the present work the simulation emulates that the PALS-retrofitted full car experiences a smooth speed bump with the height of 5 cm and the traverse distance of 2 m at a constant driving speed. The rear axle has a travel distance delay of the wheelbase ($b_f + b_r$) with respect to the front wheels. The road heights for front ($h_f$) and rear ($h_r$) wheels against the traveled distance ($x$) are:

$$h_f = 0.025(1 - \cos \pi x),$$
$$h_r = 0.025\big(1 - \cos \pi (x - b_f - b_r)\big). \tag{27}$$

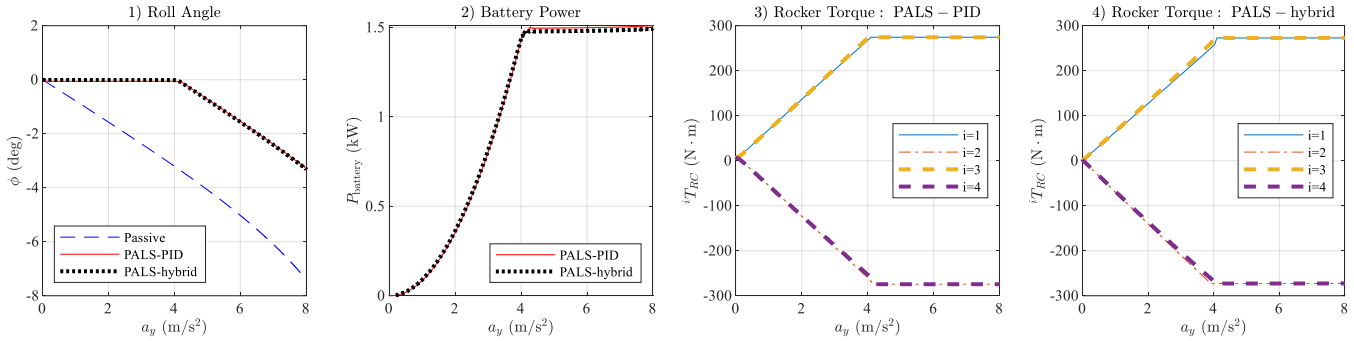


Fig. 12. Numerical simulation results with ISO steady-state cornering maneuver: variables depicted are 1) the chassis roll angle, 2) the total power consumption in the DC batteries, 3) the rocker torque at each corner with the control scheme "PALS-PID", and 4) the rocker torque at each corner with the control scheme "PALS-hybrid".

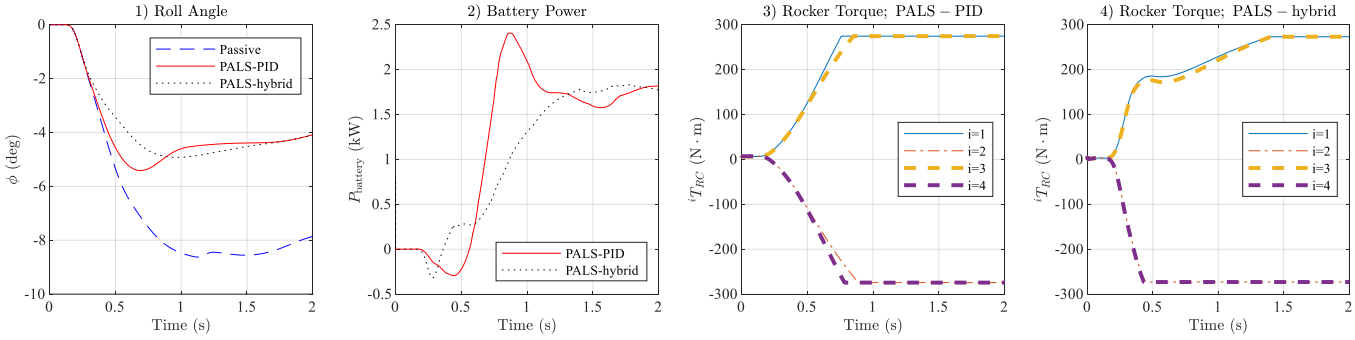


Fig. 13. Numerical simulation results with ISO step steer maneuver: variables depicted are 1) the chassis roll angle, 2) the total power consumption in the DC batteries, 3) the rocker torque at each corner with the control scheme "PALS-PID", and 4) the rocker torque at each corner with the control scheme "PALS-hybrid".

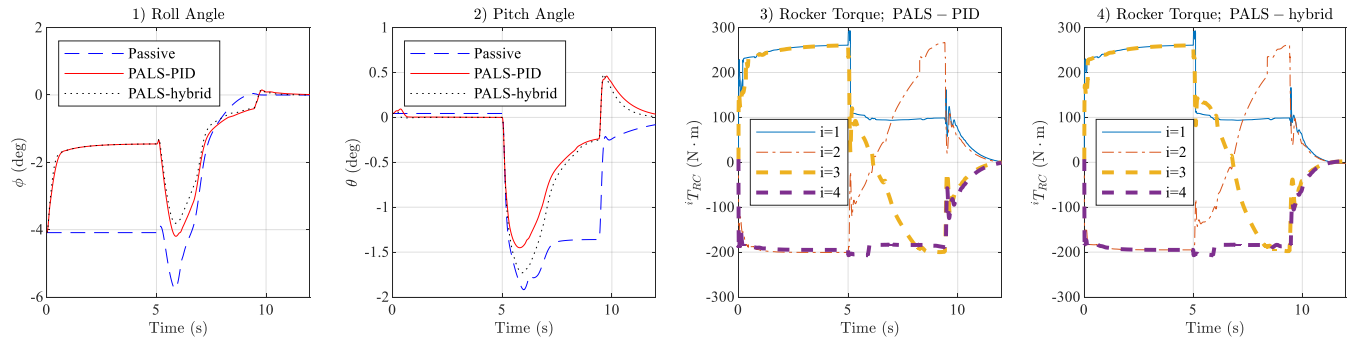


Fig. 14. Numerical simulation results with ISO braking in a turn maneuver: variables depicted are 1) the chassis roll angle, 2) the chassis pitch angle, 3) the rocker torque at each corner with the control scheme "PALS-PID", and 4) the rocker torque at each corner with the control scheme "PALS-hybrid".

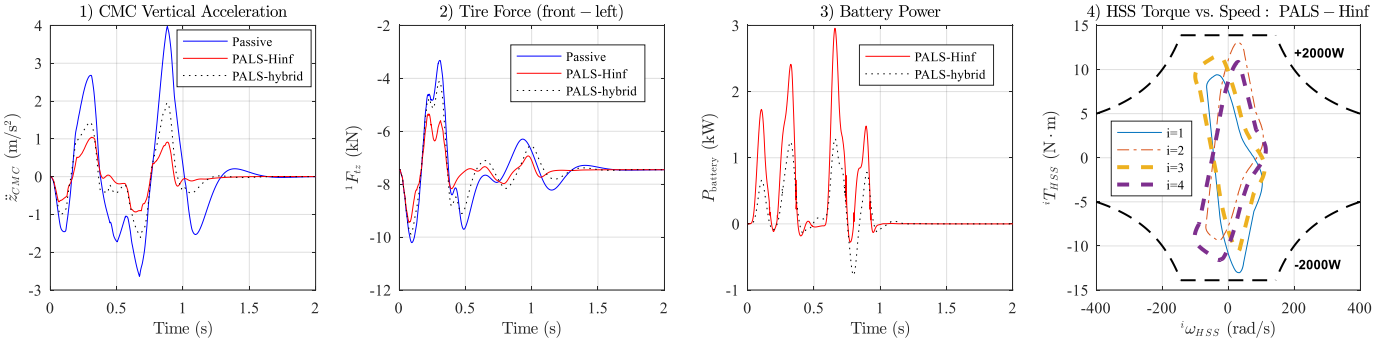


Fig. 15. Numerical simulation results with a speed bump and a constant driving speed of 20 km/h: variables depicted are 1) the CMC vertical acceleration, 2) the front-left vertical tire force, 3) the total power consumption in the DC batteries, and 4) the boundaries of torque-speed operating points of the rocker actuator HSS (high-speed shaft) at each corner ($i$ = 1, 2, 3 and 4).

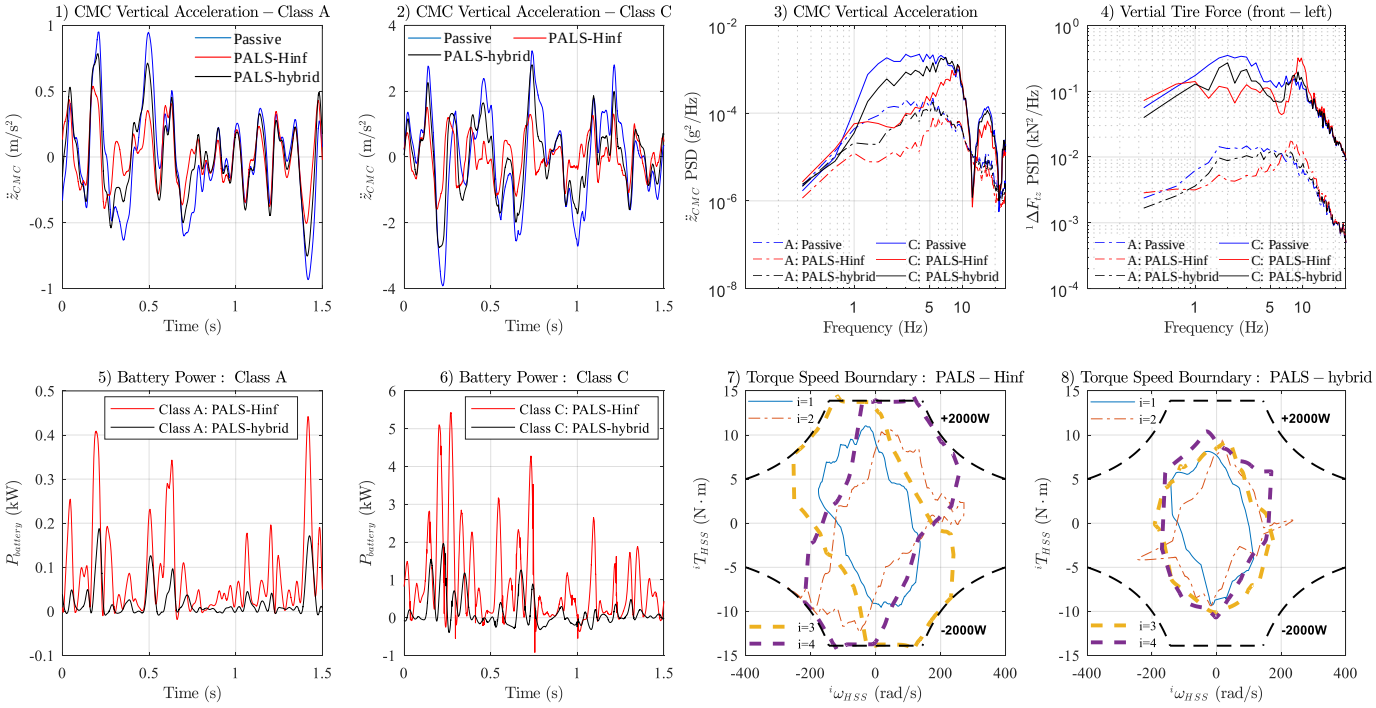


Fig. 16. Numerical simulation results with ISO random road profiles: 1)-2) depict the variation of the CMC vertical acceleration in a 1.5 s time history (out of the total simulation time of 60 s), with road Class A and Class C respectively; 3)-4) are the PSD estimates of the CMC vertical acceleration and the vertical tire force increment at the front-left corner; 5)-6) are the total consumption in the DC batteries (in the same time window as for 1) and 2)), with road Class A and Class C respectively; and 7)-8) are the boundaries of torque-speed operating points of the rocker actuator HSS (high-speed shaft) at each corner ($i$ = 1, 2, 3 and 4), where both sets of results are with road Class C.

The ride comfort is mainly indicated by the CMC vertical acceleration ($\ddot{z}_{CMC}$), as all passengers are sitting close to the CMC position, and the road holding is mainly evaluated by the variation of the vertical tire force at each corner (${}^{i}\Delta F_{tz}$).

Numerical simulation results with the PALS-retrofitted full car at a driving speed of 20 km/h are shown in Fig. 15. The control strategy "PALS-Hinf" fully presents the PALS promising potential for vehicle vibration attenuation, as it contributes 70% and 41% reduction in the peak-to-peak value of the CMC vertical acceleration and the vertical tire force variation at each corner respectively as compared to the passive suspension, as shown in Fig. 15-1) and -2). The total power consumption in the DC batteries, $P_{battery}$, has a peak value of 3 kW (see Fig. 15-3)). The boundaries of the actuator HSS torque-speed operating points at each corner are illustrated in Fig. 15-4). Numerical simulations with the same smooth speed bump while at a higher driving speed of 40 km/h, that increases the demand on the PALS, are also performed, with the results not presented here. Despite the actuator torque and power saturate at their limit values, the PALS still reduces the peak-to-peak value of the CMC vertical acceleration and the vertical tire force variation by 59% and 11% respectively, as compared to the passive suspension, further indicating its potential.

In contrast, the frequency-dependent multi-objective control strategy ("PALS-hybrid") compromises the ride comfort and road holding improvement, as compared to the "PALS-Hinf", although its performance improvement over the passive suspension is still significant especially for the CMC vertical acceleration. Furthermore, it consumes somewhat less power as compared to the "PALS-Hinf", with lower positive power values and larger negative (regenerative) power values in the DC batteries.

### *E. Case Study with Random Road*

The ISO random roads are constructed according to [33], where measured vertical surface profile data from streets, roads, highways and off-road terrain are mathematically described through their PSD (power spectral density), $G_d$, in the space frequency domain as follows:

$$G_d(n) = 10^{-6} \cdot 2^{2k} \cdot \left(\frac{n}{n_0}\right)^{-\omega_0}, \quad (28)$$

where $n_0$ (= 0.1 cycles/m) and $\omega_0$ (= -2) are constants, $n$ is the spatial frequency (cycles/m) and $k$ is the road roughness class. In the numerical simulation environment, two different road profiles (against driving distance) with the same roughness class are generated separately for the left and right wheels, while the real axle always has a travel distance delay of the wheelbase ($b_f + b_r$) with respect to the front axle. The PALS-retrofitted full car is driven at a constant speed of 100 km/h,

The numerical simulation results with ISO random road Class A and C are shown in Fig. 16, in which it can be seen that the "PALS-Hinf" hugely improves the ride comfort at the human comfort- and perception-sensitive frequencies (1-8 Hz). The pitch and roll accelerations (not displayed here) have a relatively small magnitude and are therefore of low importance for the random road cases. The average value of the total power consumption, $P_{battery}$, is 0.93 kW in the case of road Class C. The boundaries of torque-speed operating points of each rocker actuator are shown in Fig. 16-7), in which it can be seen that the power consumption of the rear two actuators is saturated at the rated value of 2 kW, while the torque variation is saturated at the (HSS) peak value Since random road driving is a long event, the operation safety of each PMSM servomotor is further evaluated. The output torque values (${}^iT_{HSS}$) are categorized to indicate the time percentage in which the actuator operates intermittently (with an HSS torque between the rated 8.3 N ṁ and peak 13.6 N ṁ values), with 0.8%, 1.6%, 15.0% and 15.1% respectively corresponding to the corner numbers of $i$ = 1, 2, 3 and 4. Moreover, the RMS values of ${}^iT_{HSS}$ for the servomotor at each corner are 3.44 N ṁ, 3.44 N ṁ, 5.42 N ṁ and 5.38 N ṁ respectively, all of which fall within the continuous duty area (0-8.3 N ṁ) and thereby are complying with the safety requirements in [25]. Therefore, the servomotor operation is considered to be safe during random road Class C driving.

Once again, the control strategy "PALS-hybrid" provides conservative control performance and consumes less power, offering a suitable performance improvement over the passive suspension. The corresponding RMS values of vertical acceleration, $\ddot{z}_{CMC}$, and the average value of $P_{battery}$ are listed in Table III in the Appendix.

## V. Conclusion

The recently proposed mechatronic suspension of the Parallel Active Link Suspension (PALS) is evaluated in the realistic application to a SUV full-car, showing promising potential for both low-frequency chassis attitude stabilization and high-frequency vehicle vibration attenuation. A general procedure for the rocker-pushrod assembly design is detailed, including the optimization of the linkage geometry and the selection of the actuation gear ratio, to maximize the rocker torque influence onto the vertical tire force increment.

An $H_\infty$ control scheme is synthesized for the PALS high-frequency application, with the ride comfort and road holding enhanced. Numerical simulations with the ISO random profiles (Class A and C) show that the CMC vertical acceleration is significantly reduced around and only around the human comfort- and perception-sensitive frequencies (1-8 Hz). Numerical simulations with a speed bump indicate 70% and 41% reduction in the peak-to-peak value of the CMC vertical acceleration and the vertical tire force respectively when driving at 20 km/h, while achieving a 59% and 11% decrease respectively at 40 km/h.

The developed $H_\infty$ control is further combined with an existing multi-objective PID control [18] in a unified scheme to fulfill all the functions of the PALS, as would be required in a real application. The synthesized hybrid control is demonstrated to exhibit the same steady-state suspension performance as the pure PID control does. This is because the tracking errors between the control outputs of the PID and the $H_\infty$ control parts can be zeroed by the designed hybrid control scheme. In contrast, as compared to the pure $H_\infty$ control, a performance compromise in terms of both ride comfort and road holding has to be made, due to the moderate interference at higher frequencies by the PID part in the hybrid control scheme and the conflict between multiple performance objectives. As compared to the passive suspension, this frequency-dependent multi-objective control scheme, on one hand, moderately improves both the ride comfort and the road holding at their frequencies of interest, and on the other hand, stabilizes the rocker torque at each corner to its reference value to achieve a desirable chassis attitude at low frequencies.

Overall, the work presented in this paper shows the promising potential of the PALS in the full car application. Also, the control strategies development and implementation provide a solid foundation for upcoming on-road experimental tests.

# APPENDIX

TABLE I
MAIN PARAMETERS OF ORIGINAL VEHICLE AND PALS RETROFIT

| **Parameters** | **Axle** | **Vaule** | **Unit** |
|---|---|---|---|
| Original vehicle (SUV) | | | |
| Total/sprung mass | - | 2950/2700 | kg |
| Wheelbase/CMC height | - | 3076/710 | mm |
| Trackwidth | F/R | 1677/1696 | mm |
| Weight distribution | F/R | 50/50 | % |
| Suspension spring stiffness ($^{i}k_{SD}$) | F/R | 150/200 | kN/m |
| Tire stiffness ($^{i}k_{t}$) | F&R | 290 | kN/m |
| Tire damping ($^{i}c_{t}$) | F&R | 300 | N/(m/s) |
| Installation ratio | F/R | 0.58/0.50 | - |
| Linear equivalent model | | | |
| Linearized suspension stiffness ($^{i}k_{eq}$) | F/R | 53.6/53.1 | kN/m |
| Linearized suspension damping ($^{i}c_{eq}$) | F/R | 2356/2002 | N/(m/s) |
| PALS retrofit | | | |
| Rocker length | F/R | 65.6/63.5 | mm |
| Pushrod length | F/R | 211.0/194.4 | mm |
| Gear ratio | F/R | 20/20 | - |
| Actuator mass | F&R | 7.4* | kg |
| Total mass increment** | - | 70 | kg |
| LSS continous torque | F/R | 166/165 | N·m |
| LSS peak torque | F/R | 273/273 | N·m |

* 7.4 kg is the mass of the Wittenstein integarted actuator comprising both the motor and the gearbox (TPM+ power 010 series [25]);
** The total mass increment with respect to the original vehicle takes into account: the motor, the gearbox, the bearings, the linkages and the servo drive at each corner, as well as relevant electronic devices.

TABLE II
PID TUNING PARAMETERS IN "PALS-PID" AND "PALS-HYBRID" CONTROL SCHEMES

| ***Parameters*** | ***Axle*** | ***Symbol*** | ***Unit*** | ***Value (PALS-PID)*** | ***Value (PALS-hybrid)*** |
|---|---|---|---|---|---|
| pitch proportional | F/R | $K_{p,f}^{(1)}/K_{p,r}^{(1)}$ | (N·m)/(rad/s) | 2000/2000 | 1000/1000 |
| pitch integral | F/R | $K_{i,f}^{(1)}/K_{i,r}^{(1)}$ | (N·m)/rad | 20000/20000 | 5000/5000 |
| pitch derivative | F/R | $K_{d,f}^{(1)}/K_{d,r}^{(1)}$ | (N·m)/(rad/s$^2$) | 4/4 | 4/4 |
| roll proportional | F/R | $K_{p,f}^{(2)}/K_{p,r}^{(2)}$ | (N·m)/(rad/s) | 500/500 | 500/500 |
| roll integral | F/R | $K_{i,f}^{(2)}/K_{i,r}^{(2)}$ | (N·m)/rad | 5000/5000 | 2500/2500 |
| roll derivative | F/R | $K_{d,f}^{(2)}/K_{d,r}^{(2)}$ | (N·m)/(rad/s$^2$) | 4/4 | 4/4 |

TABLE III
KEY PERFORMANCE OBJECTIVES AND AVERAGE POWER CONSUMPTION WITH DIFFERENT ROAD CASES

| | ***Passive*** | ***PALS-PID*** | ***PALS-Hinf*** | ***PALS-hybrid*** |
|---|---|---|---|---|
| **Road case 1: steady-state cornering** | | | | |
| peak-to-peak ($\phi$) | 7.6 deg | 3.7 deg (51%)* | - | 3.7 deg (51%) |
| average ($P_{battery}$) | 0 kW | +1.25 kW | - | +1.25 kW |
| max ($P_{battery}$) | 0 kW | +1.51 kW | - | +1.51 kW |
| **Road case 2: step steer** | | | | |
| RMS ($\phi$) | 7.1 deg | 4.1 deg (42%) | - | 4.0 deg (44%) |
| average ($P_{battery}$) | 0 kW | +1.18 kW | - | +0.77 kW |
| **Road case 3: braking in a turn** | | | | |
| RMS ($\phi$) | 3.3 deg | 1.8 deg (45%) | - | 1.7 deg (48%) |
| RMS ($\theta$) | 0.9 deg | 0.5 deg (44%) | - | 0.6 deg (33%) |
| average ($P_{battery}$) | 0 kW | +0.61 kW | - | +0.57 kW |
| **Road case 4: speed bump** | | | | |
| peak-to-peak ($\ddot{z}_{CMC}$) | 6.61 m/s$^2$ | - | 1.98 m/s$^2$ (70%) | 3.56 m/s$^2$ (46%) |
| peak-to-peak ($^i\Delta F_{tz}$) | 6.89 kN | - | 4.09 kN (41%) | 5.78 kN (16%) |
| average ($P_{battery}$) | 0 kW | - | +0.67 kW | +0.27 kW |
| **Road case 5: random road class A** | | | | |
| RMS ($\ddot{z}_{CMC}$) | 0.33 m/s$^2$ | - | 0.20 m/s$^2$ (39%) | 0.27 m/s$^2$ (18%) |
| average ($P_{battery}$) | 0 kW | - | +0.08 kW | +0.02 kW |
| max ($P_{battery}$) | 0 kW | - | +1.00 kW | +0.23 kW |
| min ($P_{battery}$) | 0 kW | - | -0.02 kW** | -0.02 kW |
| **Road case 6: random road class C** | | | | |
| RMS ($\ddot{z}_{CMC}$) | 1.15m/s$^2$ | - | 0.61 m/s$^2$ (47%) | 0.94 m/s$^2$ (18%) |
| average ($P_{battery}$) | 0 kW | - | +0.93 kW | +0.18 kW |
| max ($P_{battery}$) | 0 kW | - | +8.23 kW | +2.44 kW |
| max ($P_{battery}$) | 0 kW | - | -2.36 kW | -0.97 kW |

* Numbers in the brackets are the performance improvement percentages over the passive case;
** Negative numbers mean that the overall PALS system is charging the DC batteries.

## REFERENCES


[1] The Crazy Bose 'Magic Carpet' Car Suspension System Is Finally Headed For Production [Online]. Available: https://www.thedrive.com/news/20996/the-crazy-bose-magic-carpet-car-suspension-system-is-finally-headed-for-production

[2] Michelin to Commercialize Active Wheel [Online]. Available: https://www.michelin.com/

[3] The Magic Body Control suspension system, Mercedes-Benz [Online]. Available: https://www.mercedes-benz.co.uk/passengercars/mercedes-benz-cars/models/s-class/saloon-w222/comfort/chassis.module.html

[4] The AIRMATIC air suspension system, Mercedes-Benz [Online]. Available: www.mercedes-benz.com

[5] Tesla Model S Features, Tesla Motors [Online]. Available: www.teslamotors.com

[6] Multifaceted personality: predictive active suspension in the A8 flagship model, Audi [Online]. Available: www.audi-mediacenter.com

[7] H. Gao, W. Sun and P. Shi, "Robust Sampled-Data H-infinity Control for Vehicle Active Suspension Systems," *IEEE Transactions on Control Systems Technology*, vol. 18, no. 1, pp. 238-245, Jan. 2010.

[8] T. van der Sande, B. Gysen, I. Besselink, J. Paulides, E. Lomonova, and H. Nijmeijer, "Robust control of an electromagnetic active suspension system: Simulations and measurements," *Mechatronics*, vol. 23, no. 2, pp. 204–212, 2013.

[9] M. C. Smith and Fu-Cheng Wang, "Controller parameterization for disturbance response decoupling: application to vehicle active suspension control," in *IEEE Transactions on Control Systems Technology*, vol. 10, no. 3, pp. 393-407, May 2002.

[10] C. Gohrle, A. Schindler, A. Wagner, and O. Sawodny, "Design and vehicle implementation of preview active suspension controllers," *IEEE Transactions on Control Systems Technology*, vol. 22, no. 3, pp. 1135–1142, May 2014.

[11] M. Canale, M. Milanese and C. Novara, "Semi-Active Suspension Control Using "Fast" Model-Predictive Techniques," *IEEE Transactions on Control Systems Technology*, vol. 14, no. 6, pp. 1034-1046, Nov. 2006.

[12] J. J. Rath, M. Defoort, H. R. Karimi and K. C. Veluvolu, "Output Feedback Active Suspension Control With Higher Order Terminal Sliding Mode," *IEEE Transactions on Industrial Electronics*, vol. 64, no. 2, pp. 1392-1403, Feb. 2017.

[13] H. Kim and H. Lee, "Height and Leveling Control of Automotive Air Suspension System Using Sliding Mode Approach," *IEEE Transactions on Vehicular Technology*, vol. 60, no. 5, pp. 2027-2041, Jun 2011.

[14] H. Kim and H. Lee, "Fault-Tolerant Control Algorithm for a Four-Corner Closed-Loop Air Suspension System," *IEEE Transactions on Industrial Electronics*, vol. 58, no. 10, pp. 4866-4879, Oct. 2011.

[15] B. Németh, D. Fényes, P. Gáspár and J. Bokor, "Coordination of Independent Steering and Torque Vectoring in a Variable-Geometry Suspension System," *IEEE Transactions on Control Systems Technology*, vol. 27, no. 5, pp. 2209-2220, Sept. 2019.

[16] M. Čorić, D. Joško, L. Xu, H.E. Tseng, and D. Hrovat. "Optimisation of active suspension control inputs for improved performance of active safety systems." *Vehicle system dynamics*, vol. 56, no. 1 pp. 1-26, 2018.

[17] M. Yu, C. Arana, S. A. Evangelou, D. Dini and G. D. Cleaver, "Parallel active link suspension: a quarter car experimental study," *IEEE/ASME Transactions on Mechatronics*, vol. 23, no. 5, pp. 2066-2077, 2018.

[18] M. Yu, S. A. Evangelou, and D. Dini, "Chassis leveling control with parallel active link suspension," *the 14th International Symposium on Advanced Vehicle Control (AVEC)*, Beijing, China, 2018.
[19] M. Yu, S. A. Evangelou and D. Dini, "Position Control of Parallel Active Link Suspension with Backlash," *IEEE Transactions on Industrial Electronics*, vol. 67, no. 6, pp. 4741-4751, June 2020.
[20] C. Arana, S. A. Evangelou, and D. Dini, "Series active variable geometry suspension for road vehicles," *IEEE/ASME Transactions on Mechatronics*, vol. 20, no. 1, pp. 361–372, Feb. 2015.
[21] C. Arana, S. A. Evangelou, and D. Dini, "Series active variable geometry suspension application to chassis attitude control," *IEEE/ASME Transactions on Mechatronics*, vol. 21, no. 1, pp. 518–530, Feb. 2016.
[22] M. Yu, C. Arana, S. A. Evangelou and D. Dini, "Quarter-car experimental study for series active variable geometry suspension," *IEEE Transactions on Control Systems Technology*, vol. 27, no. 2, pp. 743-759, March 2019.
[23] M. Nordin and P. Gutman, "Controlling mechanical systems with backlash—a survey," *Automatica*, vol. 38, (10), pp. 1633-1649, 2002.
[24] Anon. (1998). *AutoSim 2.5+ Reference Manual*, Mechanical Simulation Corporation, Ann Arbor MI, USA. [Online]. Available: http://www.carsim.com
[25] Wittenstein TPM+ Rotary Servo Actuators, Wittenstein ltd, Staffordshire, UK. [Online]. Available: https://www.wittenstein.co.uk
[26] Micron True Planetary Gearheads, UltraTrue™ Series, Thomson Corp., Radford, VA, USA. [Online]. Available: http://www.thomsonlinear.com
[27] P. Pillay and R. Krishnan, "Modeling of permanent magnet motor drives," *IEEE Transactions on Industrial Electronics*, vol. 35, no. 4, pp. 537-541, Nov. 1988.
[28] K. Zhou and J. C. Doyle, *Essentials of Robust Control*. Upper Saddle River, NJ, USA: Prentice-Hall, 1998.
[29] ISO, *4138: 2004, Passenger Cars—Steady-State Circular Driving Behaviour—Open-Loop Test Methods*, Geneva, Switzerland, 2004.
[30] ISO, *7401: 2011, Road Vehicles—Lateral Transient Response Test Methods—Open-Loop Test Methods*, Geneva, Switzerland, 2011.
[31] ISO, *7975: 2006, Passenger Cars—Braking in a Turn–Open-Loop Test Method*, Geneva, Switzerland, 2006.
[32] ISO, *2631-1: 1997, Mechanical Vibration and Shock: Evaluation of Human Exposure to Whole-Body Vibration. Part 1, General Requirements*, 1997.
[33] ISO, *8608: 2016, Mechanical vibration-Road surface profiles-Reporting of measured data*, 2016.